Forecasting Storm Surge and Inundation: Model Validation

JAYARAM VEERAMONY

Naval Research Laboratory, Stennis Space Center, Mississippi

ANDREW CONDON

U.S. Army Corps of Engineers Jacksonville District, Jacksonville, Florida

MAARTEN VAN ORMONDT

Deltares, Delft, Netherlands

ABSTRACT

Coastal regions are increasingly vulnerable to damage from storm surge and inundation. Delft3D is used by the Naval Oceanographic Office to model the ocean dynamics in the near shore. In this study, the performance of Delft3D in predicting the surge and inundation during Hurricane Ike, which impacted the northern Gulf of Mexico in September 2008, is examined. Wave height, water level, and high-water mark comparisons with a number of observations confirm that the model does well in predicting the surge and inundation during extreme events. The impact of using forecast winds based on the best-track data as opposed to hindcast winds is also investigated, and it is found that the extent of inundation is represented reasonably well with the forecast winds. In Delft3D, waves can be coupled to the hydrodynamic component using the radiation stress gradient method or the dissipation method. Comparing the results of using the two shows that for low-resolution grids such as that needed for a forecast model the dissipation method works better at reproducing the water levels and inundation.

1. Introduction

With increased storm activity in recent times, coastal regions are increasingly vulnerable to storm surge and inundation. It is estimated that 10% of the world population lives in the 2% of the total landmass of the earth that composes the low-elevation coastal zone (LECZ), which is the land area contiguous with the coast that is 10 m or less in elevation (Oliver-Smith 2009). These low-lying regions are at most risk from storm surge and coastal inundation, and it is critical to provide accurate and timely forecasts of coastal inundation.

A number of storm surge modeling systems such as the Advanced Circulation (ADCIRC) model (Hope et al. 2013; Kerr et al. 2013b), Curvilinear-Grid Hydrodynamics 3D Model–Storm Surge Modeling System (CH3D-SSMS; Sheng et al. 2010a,b), the Coastal Marine Environmental Prediction System (CMEPS; Xie et al. 2004, 2008), the Eulerian–Lagrangian Circulation model (ELCIRC; Zhang et al. 2004; Wang et al. 2005), the Finite-Volume, Primitive Equation Community Ocean Model (FVCOM; Weisberg and Zheng 2008), and the Princeton Ocean Model (POM; Peng et al. 2004) have been used to model surge and inundation in coastal areas due to tropical storms. The Delft3D modeling suite (Lesser et al. 2004) is currently used by the Naval Oceanographic Office for nearshore applications and more recently to forecast surge and inundation (Veeramony et al. 2014) in their Coastal Surge and Inundation Prediction System (CSIPS). It is a fully integrated software suite for two-dimensional (2D) and three-dimensional (3D) computations for coastal, river, and estuarine areas. It is a robust model for regional and nearshore applications, and the time to set up the model for any event-based forecast for any region is on the order of minutes using the open-source tool Delft Dashboard (de Boer et al. 2012).

In this study, we look at the performance of Delft3D when modeling surge and inundation during Hurricane Ike, which impacted the northern Gulf of Mexico in

Corresponding author: Jayaram Veeramony, jay.veeramony@nrlssc.navy.mil

September 2008. Ike provides an ideal test case for CSIPS due to the large storm surge along the Texas and Louisiana coastlines and the wealth of data collected. The synopsis of Hurricane Ike has been reported in a number of publications (Rego and Li 2010; Hope et al. 2013). In addition to the surge at landfall, there was a large forerunner surge along the Louisiana–Texas coast 12–24 h prior to landfall (Kennedy et al. 2011b) that was significantly larger at some locations than the surge. A number of National Ocean Services (NOS) tide stations, located throughout the northwestern Gulf of Mexico, captured the surge event with time series of water levels and winds. Surge in excess of 1.5 m was found along the central Louisiana coast, increasing to over 3 m along the southwestern Louisiana coast. The highest NOS gauge-recorded surge was at Sabine Pass North, in Texas, near the Louisiana border [4.07 m above mean sea level (MSL)]. Water levels reached even higher across the Bolivar Peninsula where U.S. Geological Survey (USGS) sensors (East et al. 2008) and poststorm high-water mark analysis from the Federal Emergency Management Agency (FEMA 2009) showed inundation reaching around 4.5 m MSL. Along with the water-level data, Ike passed by a number of National Data Buoy Center (NDBC) Coastal-Marine Automated Network (C-MAN) buoys, which recorded wave and wind data. As a result of this large collection of data and the destructive nature of the storm, Ike has also been well studied (East et al. 2008; FEMA 2009; Rego and Li 2010; Kennedy et al. 2011a,b; Bender et al. 2013; Kerr et al. 2013b), providing high-resolution datasets and analysis techniques for our research.

All models mentioned earlier are complex and have a number of assumptions and parameterizations, since it is impossible to compute all relevant physical quantities given the restrictions on computational resources and time to solution for any given forecast. A number of studies have looked at the impact of various parameterizations such as bottom friction, wind drag, model resolutions, wave influence, and wave–current interactions (see, e.g., Kennedy et al. 2011b; Kerr et al. 2013a; Sheng et al. 2010b; Xie et al. 2008; among others). Delft3D is unique in the way waves can be coupled to the circulation with the use of the dissipation method (Dingemans et al. 1987), as well as the more traditional radiation stress gradient method. Furthermore, changes in morphology that result from wave and current activity can also be included in the simulations. Significant changes in morphology occur during the passage of storms due to erosion, resulting in changes in nearshore bathymetry and the possible destruction of protective sand dunes and other structures, which, in turn, can

result in much higher surge and flooding than would be the case if the bathymetry/topography were unchanged for the duration of the storm. However, this topic is beyond the scope of the current study; we therefore choose to ignore the effects of changes in morphology and concentrate on the wave and hydrodynamic components. In forecasting surge and inundation, one limitation (among others) that needs to be addressed is that typically an analyzed wind field is not available until the storm has passed. In this article we first analyze the performance of the Delft3D system and then look at the impact of using forecast winds versus hindcast winds to predict storm surge and also the differences between the two methods of coupling between waves and circulation as modeled in Delft3D.

2. The Delft3D model

The Delft3D modeling suite is composed of several modules that can simulate hydrodynamic flows (Delft3d-FLOW, FLOW for short), waves (Delft3d-WAVE, WAVE for short), sediment transport (Delft3d-SED), and water quality (Delft3d-WAQ). FLOW is a multidimensional hydrodynamic simulation program that calculates nonsteady hydrodynamic flow that results from external forcings such as winds, tides, and waves on a rectilinear or curvilinear boundary fitted grid. In our applications for the simulation of storm surge and inundation, we use this model in 2D mode only, since tests have indicated that the increased computational effort for 3D simulations yields little to no additional information. This is primarily due to the well-mixed upper-ocean boundary layer that can extend downward up to 100 m on the continental shelf during the passage of tropical systems (Hope et al. 2013). FLOW solves the Navier–Stokes equations for an incompressible fluid under shallow water and Boussinesq assumptions. In 2D mode, the depth-averaged continuity equation is solved along with the momentum equations in the horizontal directions. Hydrostatic pressure is assumed, and vertical accelerations due to buoyancy and sudden changes in bottom topography are not taken into account.

WAVE is a wrapper that enables the coupling of the third-generation finite-difference Simulating Waves Nearshore (SWAN) model (Holthuijsen et al. 1993; Booij et al. 1999; Ris et al. 1999) to FLOW. SWAN is a phase-averaged wave model that is used to simulate the evolution of random, short-crested wind waves. It is based on the discrete spectral action balance equation and accounts for refraction due to currents and bottom topography, dissipation due to whitecapping, depth-limited wave breaking, and bottom friction, as well as nonlinear wave–wave interactions. The version of
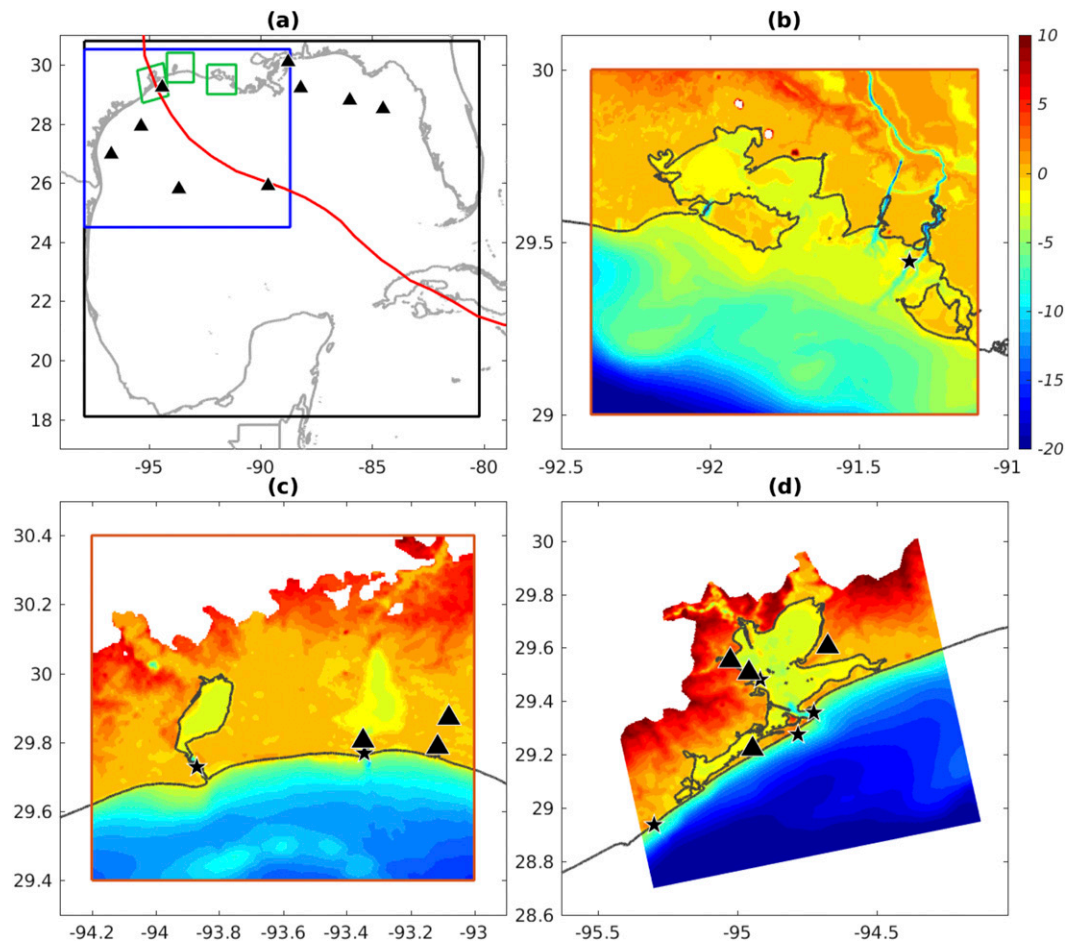
FIG. 1. Model domains used in this study. (a) Track for Hurricane Ike (red line) with the wave buoy locations (filled triangle), the GoM domain (black box), NGoM domain (blue box), and the local domains (green boxes). (b)–(d) Local domains from (a) along with the NOS water-level stations (stars) and USGS deployments (filled triangles) used in this article and the water depth ranging from −20 m (underwater) to 10 m.

SWAN used here includes the new wave dissipation mechanism described in Rogers et al. (2012), which ensures that wave components only break when their steepness exceeds a minimum threshold calculated from the saturation spectrum defined by Phillips (1984) and also includes the effects of the dissipation of short waves in the presence of longer waves. When FLOW and WAVE are run in coupled mode, they are linked dynamically where the FLOW module passes to WAVE the currents, the water levels, winds, and any changes in topography (if the Delft3D-SED is included in the coupling), and WAVE passes to FLOW the wave orbital velocity as well as wave forces.

3. Model setup

The model was run in nested mode with a total of five domains used (Fig. 1a). The large-scale domain covered the Gulf of Mexico (GoM) with a resolution of 0.1° (approximately 10 km), consisting of 22 784 (178 × 128) grid cells. Nested within the GoM domain was a regional domain that covered much of the northern Gulf (NGoM) from the Texas coast to the mouth of the Mississippi River with a resolution of 0.02° (approximately 2 km) and consisting of 138 761 cells (461 × 301). Within this regional domain were three coastal domains with a resolution of 0.004° (approximately 400 m). These coastal domains covered the Vermillion Bay (VB) area of Louisiana (Fig. 1b), the Port Arthur (PA) area along the Texas–Louisiana border (Fig. 1c), and Galveston Bay (GB) (Fig. 1d), respectively. The VB domain has 81 826 cells (326 × 251), the PA domain features 75 551 cells (301 × 251), and the GB domain features 84 581 cells (301 × 281). The simulation period for the GoM domain begins at 1215 UTC 5 September 2008 and ends at 2315 UTC 14 September 2008. The conditions along

the open boundaries of inner nests are specified as a time series of the linearized Riemann invariant given by

$$R = U \pm \left(2\sqrt{gh} + \eta\sqrt{\frac{g}{h}} \right), \quad \frac{|\eta|}{h} \ll 1, \qquad (1)$$

where h is the still-water depth, η is the water level above still water, and U is the current velocity normal to the boundary calculated from the immediate outer nest. Since the Riemann boundary condition is not valid when the water surface elevation is of the same order as the water depth, along the boundaries perpendicular to the coast the normal velocity is specified. The elevation dataset used consisted primarily of bathymetry and topography gathered and made available by the Southeastern Universities Research Association (SURA) Inundation Testbed. This is a high-resolution (30 m in and around Galveston Bay) dataset available for much of the northern Gulf of Mexico. In areas where the SURA data are not available, data from the National Geophysical Data Center (NGDC) Coastal Relief Model, Shuttle Radar Topography Mission (SRTM), and General Bathymetric Chart of the Oceans (GEBCO) were used to fill in. The baseline simulation was dynamically coupled to the wave module to include wave effects. The wave simulations are much more computationally expensive than the hydrodynamic component. Tests showed that using the same grid resolution for FLOW and WAVE did not result in any appreciable increase in model skill over a reduced-resolution grid for WAVE. Therefore, for the studies presented here, the wave grid mirrored the hydrodynamic grid but with half the resolution for all domains (0.2°, 0.04°, and 0.008° for the GoM, NGoM, and GB/PA/VB domains, respectively). In the GoM and NGoM simulations, SWAN is run in nonstationary mode since waves are being actively generated in the domain because of the storm. A 12-min time step was used, with communication with the hydrodynamic model every hour. For the local domains, most of the wave energy was entering the domain via the open boundaries, and therefore the model was run in stationary mode with communication every 12 min with the hydrodynamic model. Within the hydrodynamic model the bottom roughness was calculated using the Manning formulation. To determine the values for the spatially varying Manning's N coefficient, land-use data were obtained from National Land Cover Database (NLCD) and converted into a corresponding Manning's N value based on the tables in Mattocks and Forbes (2008). Similar to the values used by Kerr et al. (2013b), for offshore areas where land-use data are nonexistent, a constant value of $0.02 \, \mathrm{s \, m^{-1/3}}$ was used for the sandy

areas around Florida and a smaller value of $0.012 \, \mathrm{s \, m^{-1/3}}$ was employed off the coast of Louisiana and Mississippi. The values around the coast are generally small but increase inland and in urban areas. The GoM and NGoM simulations were performed with a time step of 30 s, and the coastal domains were run with a 15-s time step after experimentation addressing the stability of the simulations and convergence of the modeled values. The GoM domain required relatively smaller time steps in comparison to the NGoM domain because of the large gradients in bathymetry near the island of Cuba. Along the open boundaries of the GoM domain, the Riemann invariants calculated from the astronomic tidal components obtained from the Oregon State University (OSU) TOPEX/Poseidon Global Inverse Solution (TPXO 7.2) tidal database (Egbert and Erofeeva 2002) were specified. A total of 13 harmonic constituents were used along with a constant value (zero phase) to account for the initial water-level conditions. Local tidal potentials were used to account for the generation of tides in the Gulf. The atmospheric forcing was provided on an equidistant grid from Oceanweather Inc. (OWI). The fields consist primarily of the NOAA H*wind (Powell et al. 1998) snapshot for the core hurricane characteristics and are then blended into background winds to create a smooth wind field. Both fields were output onto a 0.02° domain with a temporal resolution of 15 min. The winds were adjusted to account for land effects by employing a directional land-masking technique (Westerink et al. 2008). The same NLCD land-use data were used to obtain the surface roughness length z_0 values for each grid cell, and the wind field was adjusted accordingly based on the wind direction.

The atmospheric input to the coupled FLOW–WAVE system is given by the total stress:

$$\tau_{\mathrm{tot}} = C_D U_{10} \rho_a, \qquad (2)$$

of which the viscous stress,

$$\tau_\nu = C_\nu U_{10} \rho_a, \qquad (3)$$

forces the FLOW model directly, where $C_\nu = 0.0005$ is kept constant for simplicity, although an increased value of up to $C_\nu = 0.0008$ was reported by Banner and Peirson (1998) for low fetch and low wind speed. The remainder of the stress is directed toward wave generation, which releases the momentum to the ocean via dissipation. Similar to Rogers et al. (2012), we use the drag coefficient C_D from Hwang (2011):

$$C_D = (-0.016 U_{10}^2 + 0.967 U_{10} + 8.058) \times 10^{-4}, \qquad (4)$$

which is fit to the datasets of Powell et al. (2003) and Jarosz et al. (2007) and provides for saturation for wind speeds larger than $30 \, \mathrm{m \, s^{-1}}$ and even decreases at very strong speeds. To prevent the drag coefficient from dropping to zero or becoming negative at extremely high wind speeds, we apply the following limit to C_D for $U_{10} \gtrsim 50.33 \, \mathrm{m \, s^{-1}}$:

$$C_D = 4.1047 U_{10}^{-2}. \tag{5}$$

As mentioned in the previous section, when FLOW and WAVE are run in coupled mode, WAVE receives information about the currents, water levels, and winds. WAVE computes and provides to FLOW the Stokes drift, the near-bottom orbital velocity, and the wave forces. For reasons that are illustrated in section 6, the wave forces are computed based on the wave dissipation method described by Dingemans et al. (1987):

$$F_x = D \frac{k_x}{\omega} \quad \text{and} \tag{6}$$

$$F_y = D \frac{k_y}{\omega}, \tag{7}$$

where the dissipation rate D is composed of the bottom friction due to the orbital motion, whitecapping away from the shore, and depth-limited breaking close to the shore. The x and y components of the individual mechanisms are calculated in SWAN. Momentum transfer from waves to drive the ocean circulation is dominated by the whitecapping in deep water and depth-limited breaking in shallow water. The x and y components of these two mechanisms are linearly added to obtain the x and y components of the wave force.

4. Model results

Figure 2 shows comparisons of the significant wave heights, peak wave periods, and wave directions between the model and data at the buoy locations in Table 1. For a quantitative analysis of the model–data comparison, we use the following metrics:

$$\text{Bias} = \langle S - O \rangle, \tag{8}$$

$$\varepsilon = \langle |S - O| \rangle, \tag{9}$$

$$\text{RMSE} = \langle (S - O - \text{Bias})^2 \rangle^{1/2}, \tag{10}$$

$$\text{SI} = 100 \frac{\text{RMSE}}{\langle S \rangle}, \quad \text{and} \tag{11}$$

$$\text{WSS} = 1 - \frac{\sum (|S - O|)^2}{\sum (|S - \langle O \rangle| + |O - \langle O \rangle|)^2}, \tag{12}$$

with S the model results and O the observations; the angled braces $\langle \rangle$ indicate the arithmetic mean of the quantity. The quantity ε is the absolute error, RMSE is the root-mean-square error, SI is the scatter index, and WSS is the Willmott skill score (Willmott 1981) (WSS = 1 for perfect agreement between the simulation and observations and WSS = 0 for no agreement). Since we are interested in the model performance during the passage of the storm, the statistics are calculated for the 48-h period starting at 0000 UTC 12 September and ending at 0000 UTC 14 September; results are tabulated in Table 1. Based on the skill score of 0.96 or better, the agreement between the simulated and observed wave heights is excellent for all but three of the buoys (42002, 42019, and 42035). From Fig. 2 it is evident that the model overestimates the significant wave heights at the peak of the storm at these locations. However, the significant wave height biases, absolute errors, and root-mean-square errors at these buoy locations are all less than 1 m. Considering that the wave heights peaked at over 9 m at buoy 42001, these low relative errors indicate good model skill. The model skill for the wave periods is considerably lower than that for the wave heights. The simulation results show biases of generally less than 1 s, absolute errors under 2 s and root-mean-square errors mainly under 2 s, as well with a few stations around 2.6 s. The observed periods range up to 16.67 s, showing the large swells produced by Ike. Both the wave height and period statistics show low scatter index percentages and high RMSE skill scores. Overall, the wave results from the baseline simulation compare well with the observations.

The surge during Ike influenced a large area of the Texas and Louisiana coasts. In validation of the storm surge and inundation prediction system there are two different components in terms of surge and flooding. First, the model must be able to accurately predict the water level at the stations free of the interactions with land. This is a somewhat simpler task and can be commonly done at rather coarse resolutions. The harder task is to accurately simulate the surge levels that are close to land or the inundation that results from the surge. This is especially difficult because of the limitations in accuracy of the initial bathymetry, especially close to shore, as well as the large and abrupt changes in bathymetry/topography that often occur during the storm. The left panel in Fig. 3 shows the comparison between the observations and predictions of the total water level including the tidal elevation at the seven NOS stations [where the sensors are located below the mean lower low-water (MLLW) tidal datum] given in Table 2. Table 2 also gives the statistics for these locations for the
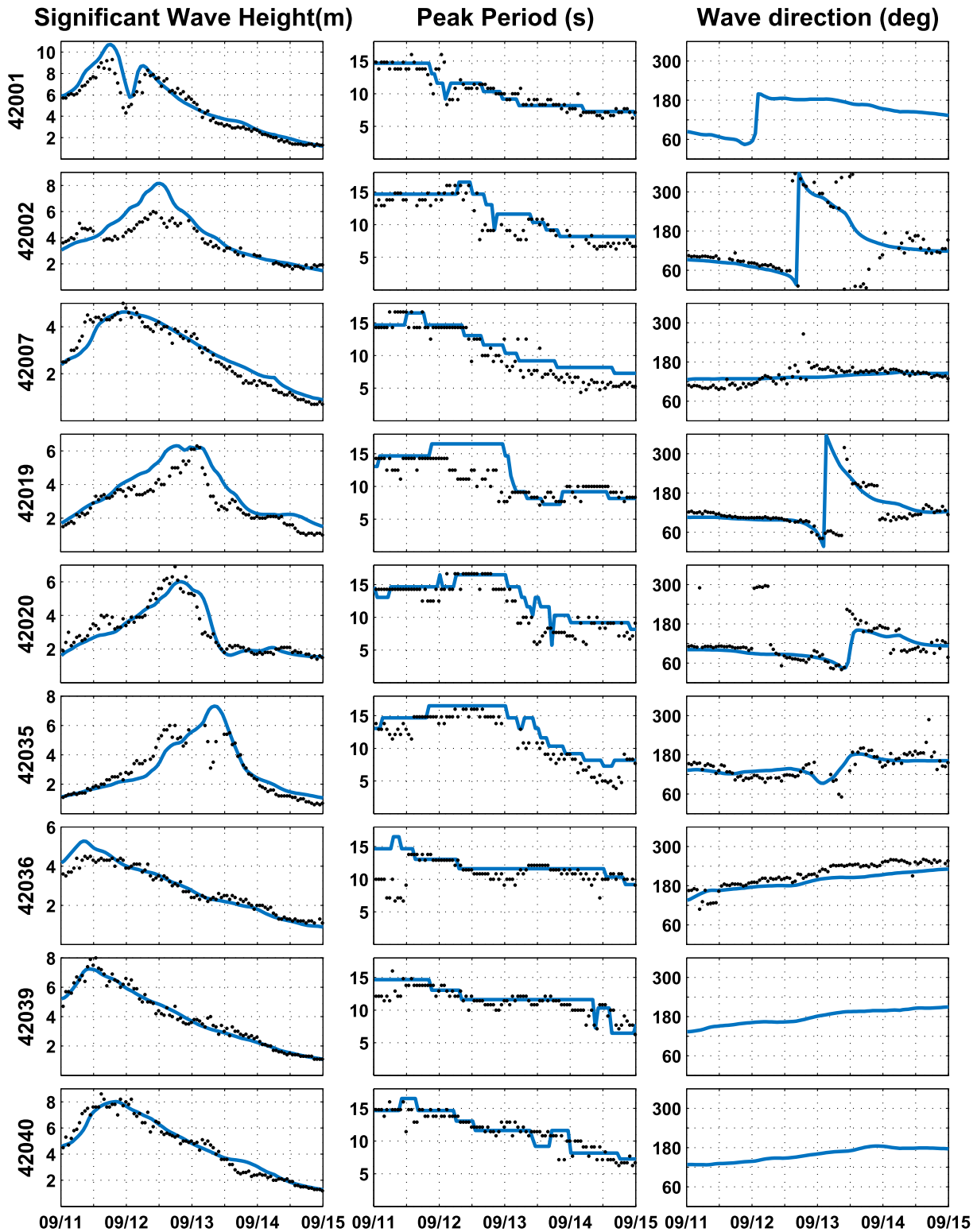
FIG. 2. Wave comparison between the model (blue line) and NDBC stations (black). Buoys 42001, 42039, and 42040 did not report wave directions.

TABLE 1. NDBC stations used in wave comparisons and performance metrics for the significant wave heights H_s and peak period T_p.

Station ID	Lat (°N)	Lon (°E)	H_s					T_p				
			Bias (m)	ε (m)	RMSE (m)	SI	WSS	Bias (m)	ε (m)	RMSE (m)	SI	WSS
42001	25.9000	−89.6670	0.22	0.48	0.58	12.58	0.98	−0.10	0.82	1.23	13.29	0.86
42002	25.7900	−93.6660	0.93	0.96	0.87	18.80	0.87	1.39	1.72	1.86	16.36	0.86
42007	30.0900	−88.7690	0.23	0.28	0.24	7.87	0.98	1.33	1.72	1.42	13.46	0.88
42019	27.9130	−95.3600	0.84	0.84	0.59	13.90	0.88	1.96	2.56	2.90	24.23	0.65
42020	26.9660	−96.6950	0.05	0.43	0.61	17.41	0.96	1.60	1.85	1.92	14.73	0.87
42035	29.2320	−94.4130	0.02	0.81	1.16	29.57	0.86	1.76	1.76	1.01	7.66	0.92
42036	28.5000	−84.5170	−0.07	0.18	0.20	7.91	0.98	0.67	0.85	0.94	7.97	0.60
42039	28.7910	−86.0080	−0.04	0.28	0.34	9.79	0.98	0.54	0.80	0.90	7.72	0.74
42040	29.2050	−88.2050	0.21	0.38	0.42	9.45	0.98	−0.14	0.96	1.29	11.65	0.87

relevant high-resolution local domain. For comparison, the statistics for the low-resolution GoM domain are shown in parentheses. Overall, there is good agreement between the observations and the modeled results even for the low-resolution domain. However, with one exception of the station at the Freshwater Canal Locks (8766072), the higher-resolution domains give more accurate results. The differences in the water-level predictions between the different resolutions are highest immediately after the passage of the storm. For the first two stations, which are the farthest from the center of the storm track, the lower- and higher-resolution models have nearly identical statistics. The forerunner surge is predicted better by the higher-resolution model, but the magnitude of the predicted forerunner is smaller than that observed. The right panel in Fig. 3 shows the total water-level comparisons for the USGS-deployed stations given in Table 3. These stations were deployed immediately prior to the arrival of the storm and sensor elevations were typically above the North American Vertical Datum of 1988 (NAVD88). Here, only the NGoM domain and the relevant local domain results are shown. The corresponding statistics are also given in Table 3. As can been seen in Fig. 3, the accuracy of the predictions depends to a large extent on the accuracy in bathymetry/topography. For example, in the higher-resolution model, the sensors at CHA-004 and GAL-019 are much higher above NAVD88 than the actual deployed height because of the model resolution; hence, the model does not show any inundation until the water level is higher than the elevation in the model input topography. For such cases, simulations with higher resolution are statistically worse. Figures 4a and 4b compare simulated versus observed peak water levels at all the USGS and NOS stations, respectively, including those near land. In general, the more resolved the domain, the closer the modeled

value is to the observations. To compare the model accuracy, Taylor diagrams (Taylor 2001) are shown in Figs. 4c and 4d, respectively, for the USGS and NOS stations. The standard deviation is along the radial distance from the origin, the correlation coefficient is along the azimuthal, and the centered RMSE (RMSD) calculated as in (10) is proportional to the distance from the data given by the black diamond. The GoM domain results are given by the red marker labeled G and the local domain results by the marker labeled L. For both the USGS and NOS data, the total model variance is close to the variance of the data, as illustrated by the proximity of the markers to the solid black line. The higher-resolution model is better correlated to the data and has a smaller RMSD.

The high-water mark (HWM) comparisons are presented in Fig. 5. Figure 5a shows the comparisons at the individual observations and Fig. 5b shows the overall model performance for the different resolutions. The results from the medium- (marker labeled N) and high-resolution (marker L) models are considerably better than those from the low-resolution model (marker G) in terms of the standard deviation and RMSD and also have a higher correlation to the data.

5. Impact of wind field specifications

The baseline simulation utilizes the best available hindcast winds and pressure fields. In a forecast environment, an analytic wind model must be used to generate a snapshot of the hurricane wind field based on the forecast information. In this study, we are not looking to study the impact of forecast accuracy on the surge and inundation and, therefore, will use the best-track information to develop the "forecast" wind field. We use the asymmetric wind vortex formulation presented by Mattocks and Forbes (2008), which is an adaptation of the Xie et al. (2006) model, to generate the
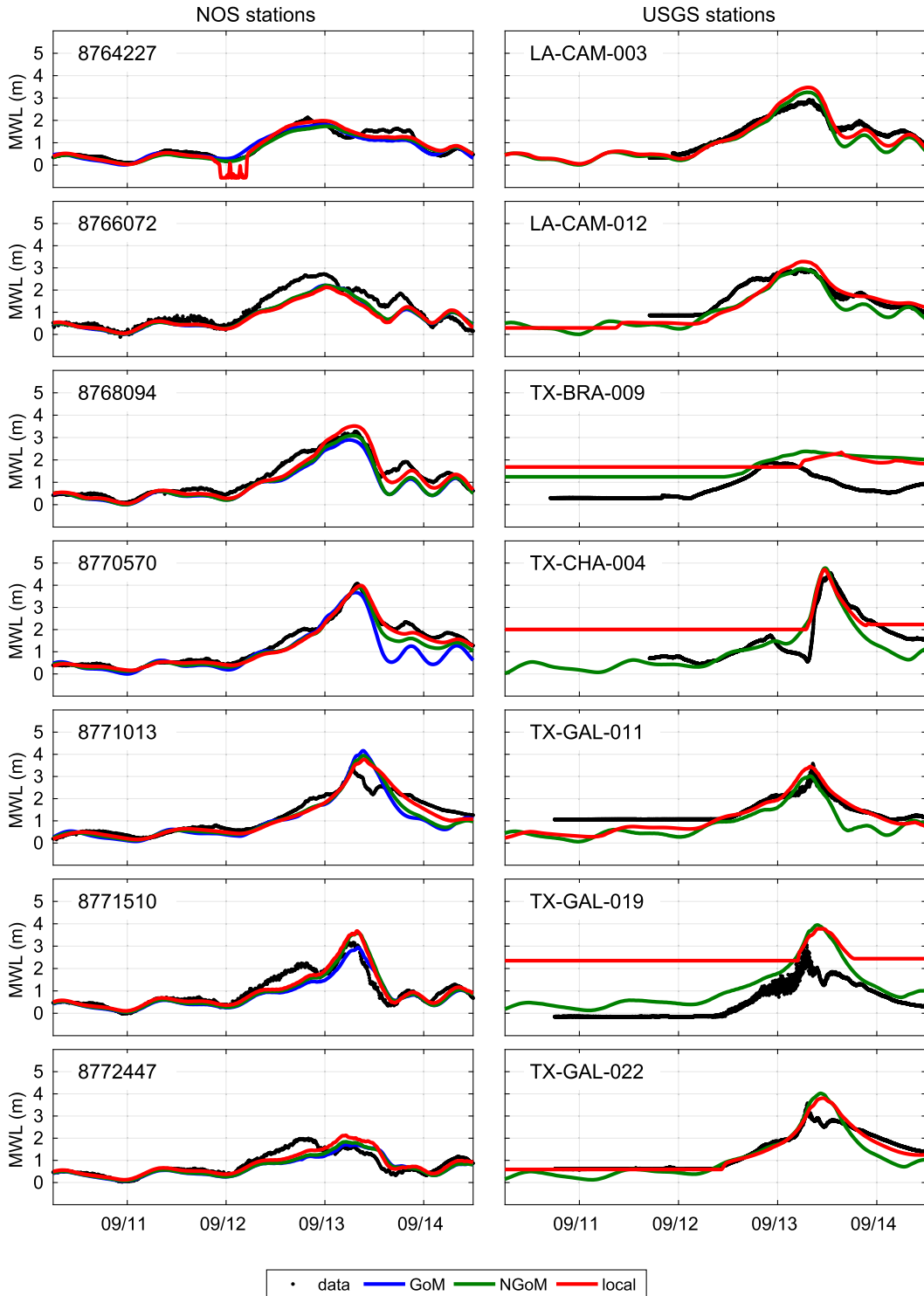
FIG. 3. Water-level comparison between model results and (left) NOS stations and (right) select USGS temporary deployments for different nests. Black dots are data, the blue line is the GoM domain, the green line is the NGoM domain, and the red line is the appropriate high-resolution domain.

TABLE 2. NOS tide stations used in water-level comparisons for Hurricane Ike and the performance metrics at each site. The values in parentheses are the statistics for the low-resolution GoM domain.

Station ID	Station name	Lat (°N)	Lon (°E)	Bias (m)	ε (m)	RMSE (m)	SI	WSS
8764227	Lawma	29.4433	−91.3300	−0.03 (−0.08)	0.22 (0.19)	0.30 (0.20)	25.84 (18.80)	0.93 (0.95)
8766072	Freshwater Canal Locks	29.7682	−93.3446	−0.38 (−0.31)	0.47 (0.39)	0.39 (0.34)	34.35 (28.82)	0.83 (0.88)
8768094	Calcasieu Pass	29.7284	−93.8701	−0.12 (−0.36)	0.29 (0.36)	0.32 (0.28)	19.52 (20.31)	0.96 (0.92)
8770570	Sabine Pass North	29.4810	−94.9170	−0.15 (−0.28)	0.21 (0.30)	0.20 (0.23)	11.45 (13.64)	0.98 (0.96)
8771013	Eagle Point	29.3570	−94.7250	−0.06 (−0.17)	0.30 (0.40)	0.39 (0.49)	23.29 (31.07)	0.94 (0.91)
8771510	Galveston Pleasure Pier	29.2755	−94.7820	−0.01 (−0.08)	0.31 (0.36)	0.40 (0.46)	29.68 (35.58)	0.93 (0.91)
8772447	USCG Freeport	28.9369	−95.2975	0.01 (−0.13)	0.29 (0.32)	0.35 (0.36)	31.83 (37.81)	0.86 (0.81)

storm wind fields. The wind speed V, as a function of radial distance r is given by

$$V(r) = \left\{ \left[\frac{B}{\rho_a} \left(\frac{R_{\max}}{r} \right)^B (P_n - P_c) \right. \right.$$
$$\left. \times\, e^{-(R_{\max}/r)^B} + \left(\frac{rf}{2} \right)^2 \right]^{1/2} - \left(\frac{rf}{2} \right) \right\}, \quad (13)$$

where B is a hurricane shape parameter, $R_{\max}$ is the radius of maximum winds, f is the Coriolis parameter, P_n is the ambient pressure, P_c is the central pressure, and ρ_a is the density of air. The shape and size of the wind field, or the peakedness, is determined by the parameter B, which is calculated from the forecast guidance as

$$B = \frac{[(V_{\max} - V_T)/W_{PBL}]^2 \rho_a e}{P_n - P_c}, \quad (14)$$

where $V_{\max}$ is the maximum sustained (1 min) wind speed in the hurricane, V_T is the storm's forward translational velocity, and W_{PBL} is a wind reduction factor. Furthermore, the condition $1 \le B \le 1.25$ is imposed to limit the shape and size of the vortex. With information on the wind speed (i.e., 34, 50, and 64 kt, where $1\,\text{kt} = 0.51\,\text{m s}^{-1}$) and the radial extent, (13) can be solved for $R_{\max}$ as a function of the four azimuthal angles

θ using a root-finding algorithm based on Brent's algorithm. The relation between $R_{\max}$ and θ is obtained using cubic splines under tension fit. Figure 6 shows the comparison of the hindcast winds and the forecast winds at 6 h prior to landfall and at landfall. Two features stand out regarding the forecast winds. The first feature is the lack of background winds, the result of which is a diminished forerunner surge, and the second feature is the much larger wind magnitudes, especially in the northeast quadrant, which leads to higher peak surge predictions. Figure 7 shows a comparison of wave heights, periods, and directions using the analytical winds. The lack of background winds is felt prior to the arrival of the storm at the data locations when the magnitudes of the significant wave heights are much lower compared with observations. At the peak of the storm, the magnitudes of the wave heights are much higher for locations along the track and to the north and east of the track and lower at locations south and west of the track. A possible solution to improve the wave predictions is to include the background winds; however, this would not impact the peak of the storm. We do find that there is a need to develop parametric models that better represent the storm structure.

We see similar tendencies in the prediction of water levels (Fig. 8). Even at the NOS stations, which are in water, there is a significant reduction in accuracy when

TABLE 3. USGS tide stations used in water-level comparisons for Hurricane Ike. The values in parentheses are as in Table 2.

Station ID	Lat (°N)	Lon (°E)	Bias (m)	ε (m)	RMSE (m)	SI	WSS
LA-CAM-003	29.8042	−93.3489	−0.02 (−0.19)	0.27 (0.32)	0.33 (0.34)	20.35 (23.26)	0.95 (0.93)
LA-CAM-012	29.7706	−93.0144	−0.08 (−0.33)	0.33 (0.34)	0.38 (0.25)	21.83 (16.81)	0.93 (0.92)
TX-BRA-009	29.0131	−95.3297	0.85 (0.90)	0.89 (0.90)	0.54 (0.48)	28.95 (25.28)	0.38 (0.46)
TX-CHA-004	29.7728	−94.6869	0.65 (−0.19)	0.75 (0.50)	0.59 (0.60)	24.98 (39.48)	0.80 (0.91)
TX-GAL-011	29.2208	−94.9447	−0.02 (−0.40)	0.21 (0.45)	0.28 (0.33)	17.98 (27.56)	0.95 (0.85)
TX-GAL-019	29.5064	−94.9578	1.76 (0.76)	1.76 (0.76)	0.54 (0.49)	21.00 (30.84)	0.44 (0.77)
TX-GAL-022	29.5517	−95.0247	0.02 (−0.13)	0.22 (0.41)	0.34 (0.54)	19.69 (33.67)	0.96 (0.90)
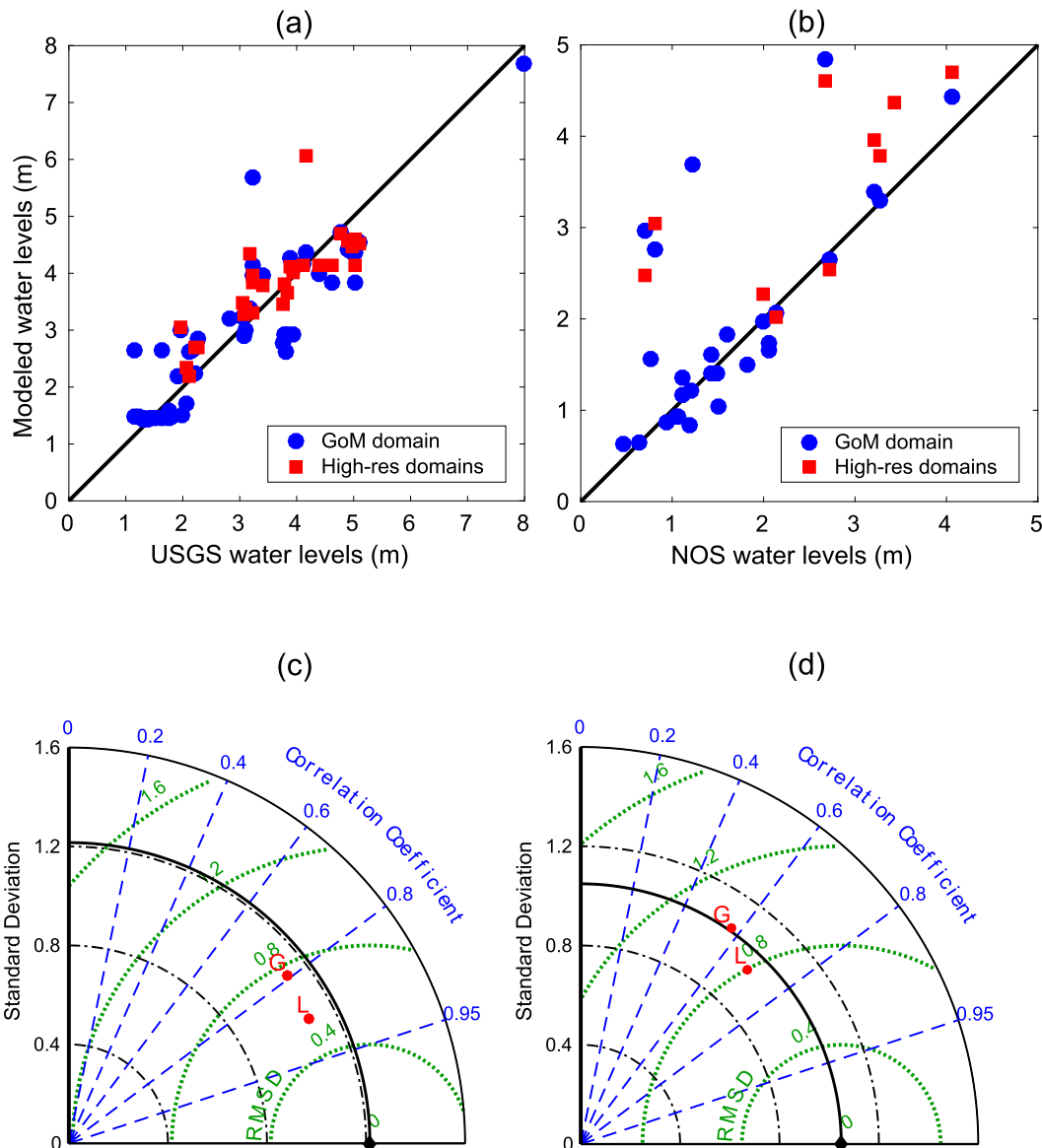
FIG. 4. Simulated vs observed peak water levels at (a) all the USGS deployments and (b) NOS stations for the GoM domain (low resolution) and the appropriate high-resolution domains. Taylor diagrams (Taylor 2001) for the (c) USGS and (d) NOS stations showing the performance of the low-resolution GoM domain (G) and high-resolution local domains (L).

predicting the peak levels. The forerunner surge is missing entirely from the simulations with forecast winds, and the water levels tend to drop off rather rapidly after the passage of the storm. Similar results are seen at the USGS stations. The results for the peak water levels and HWMs are shown in Fig. 9. The Taylor diagram illustrates the differences between the two model simulations. For the peak values, the two simulations are fairly close to each other in skill, but for the HWMs, the hindcasts show much better correlation with the data and a lot less scatter (lower RMSD

values) even though the total variances for the models are very similar and close to the measured value.

6. Wave to ocean momentum transfer

The importance of including wave forcing in surge modeling was demonstrated by a number of researchers (see, e.g., Zhang and Li 1996; Sheng et al. 2010a). Hydrodynamic and wave models running in coupled mode widely use radiation stress gradients
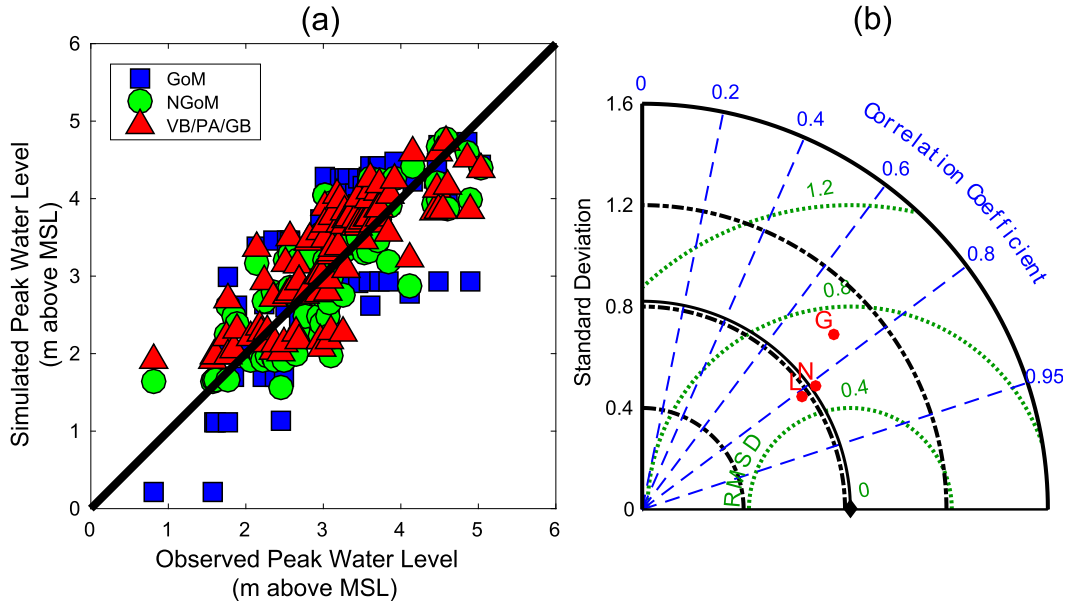
FIG. 5. (a) HWM comparison for simulations of Hurricane Ike for the different domains. (b) Taylor diagram showing the overall skill of the models: GoM domain (G), NGoM domain (N), and the local domains (L).

(Longuet-Higgins and Stewart 1964) to transfer momentum from waves to the circulation. But as pointed out by Dingemans et al. (1987), the radiation stress can have significant spatial variation and numerical differentiation can lead to significant inaccuracies. This is especially true for large-domain models with large spatial discretizations. Dingemans et al. (1987) show that the irrotational part of the radiation stresses does not contribute to the wave-driven flow, and the rotational part is closely related to the wave dissipation. Thus, the radiation stress gradients can be approximated by the wave energy dissipation. In Delft3D, wave forces can be computed using either formulation, with the 2D forcing given by

$$F_x = -\frac{\partial S_{xx}}{\partial x} - \frac{\partial S_{xy}}{\partial y} \sim D\frac{k_x}{\omega} \quad \text{and} \quad (15)$$

$$F_y = -\frac{\partial S_{xy}}{\partial x} - \frac{\partial S_{yy}}{\partial y} \sim D\frac{k_y}{\omega}. \quad (16)$$

Both the dissipation rate D as well as the radiation stresses S_{xx}, S_{yy}, and S_{xy} are computed by SWAN. Whereas the dissipation rate is due to the bottom friction because of the orbital motion, whitecapping away from the shore, and depth-limited breaking close to the shore, only the whitecapping and depth-limited breaking components transfer momentum to the ocean. Therefore, only those components are used to calculate the wave forces. The radiation stress

gradients are calculated directly from the spectra of wave energy.

Figure 10 shows the comparison between the computed water surface elevations using the hindcast winds based on the radiation stress gradients as well as the dissipation. For the NOS stations, we see that using the radiation stress gradients results in under-estimating the water level by as much as 1.5 m at locations close to the storm track. At the USGS stations, similar results are observed, with the dissipation-based wave forcing showing better agreement with the data. Figures 11a and 11b show the results for the peak water-level values and the HWMs, respectively, and Figs. 11c and 11d show the respective Taylor diagrams. In general, we see that the maximum values are underestimated by the radiation-stress-based method. However, there are a couple of locations where the peak values are overestimated by the radiation stress method, the result of which is seen in the Taylor diagram showing that the radiation stress method has variance that is closer to the data than the dissipation method. Using the HWMs shows clearly that the dissipation method has much better correspondence with the data variance than the radiation stress method. Outside the surf zone, where wave growth due to winds is almost balanced by white-capping, the net wave growth/decay is very small. Radiation stress gradients here are therefore also close to zero, but the dissipation (due to white-capping) can be very large. The dissipation method
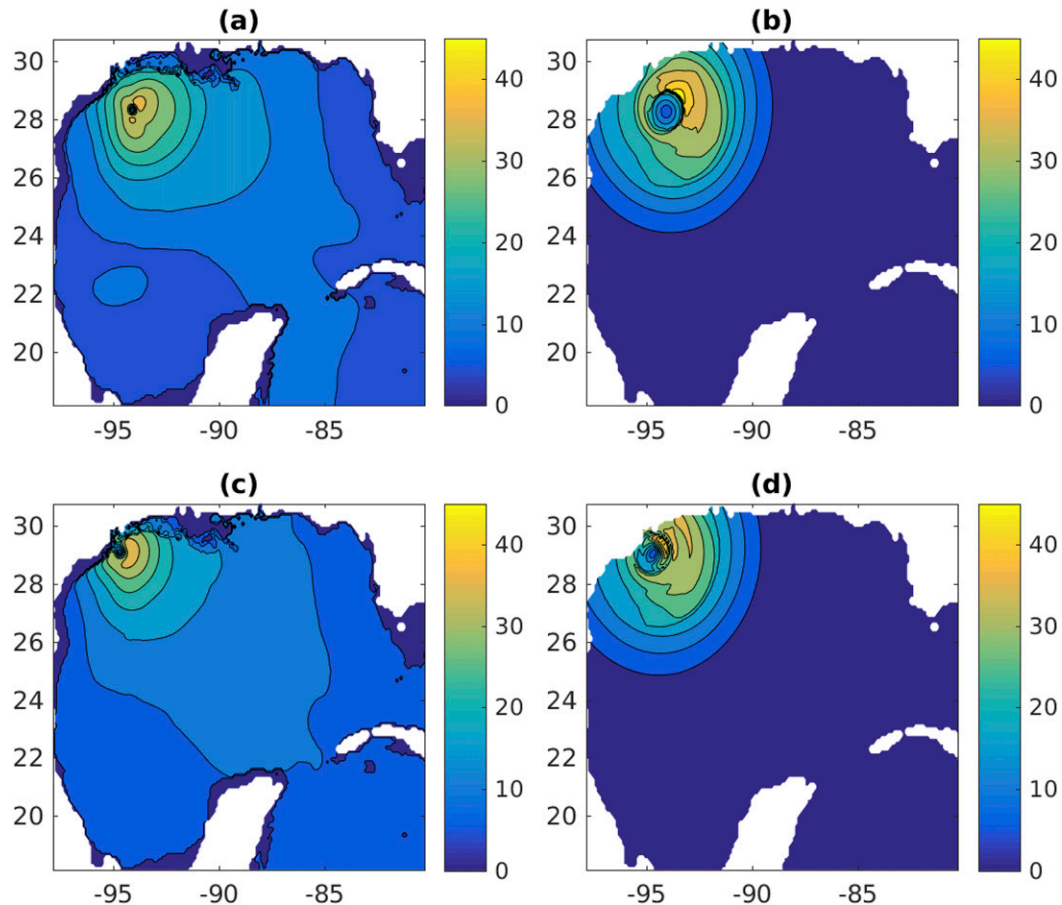
FIG. 6. Comparison of the (left) hindcast and (right) forecast wind magnitudes (m s^{-1}) at (top) 6 h prior to landfall and (bottom) landfall.

will therefore yield much higher forces in deeper water.

7. Summary and conclusions

In this study, we analyzed the performance of a coastal surge and inundation modeling system based on Delft3D, which is currently used by the Naval Oceanographic Office for nearshore applications and more recently to model surge. We simulated conditions for Hurricane Ike, which impacted the northern Gulf of Mexico in September 2008. Wave height, water level, and high-water mark comparisons with a number of observations confirm that the model did well in predicting the surge and inundation during this event. The low-resolution GoM domain gave reasonable results for the peak values of surge as well as for the HWMs. Both the medium- and high-resolution domains gave similar but better results for the peak values of surge and HMWs. The differences between

the medium- and high-resolution domains are apparent in the time series of the water levels, where the high-resolution domains do better, especially after the passage of the peak of the storm. Since for forecasts, we have to rely on the advisories that the responsible agencies provide, we also looked at the impact of using forecast winds based on the best-track data as opposed to hindcast winds. We found that the extent of the surge is represented reasonably well with the forecast winds. However, the HWMs had much lower correlation with the data, even though the overall magnitudes were predicted reasonably well, as indicated by the magnitude of the overall standard deviation. The waves were overestimated along the storm track, primarily due to the fact that the wind speeds in the analytical models are typically higher in this region. Because of a lack of background winds, the waves and water levels away from the storm track outside the storm radius were not modeled accurately. However, in most cases these areas
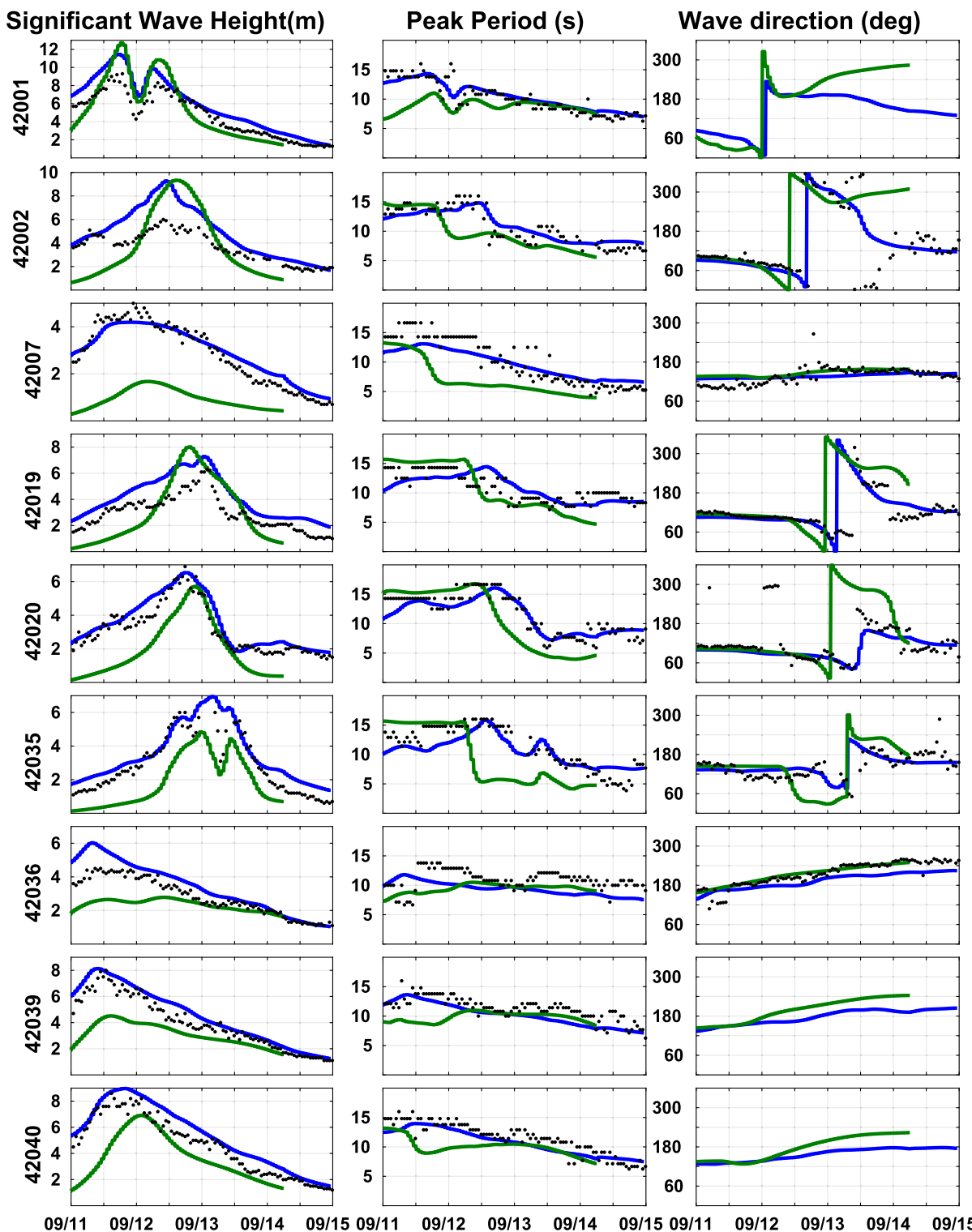
FIG. 7. Wave height, period, and direction comparison between the hindcast model (blue line), forecast model (green line), and NDBC stations (black dots). Buoys 42001, 42039, and 42040 did not report wave directions.
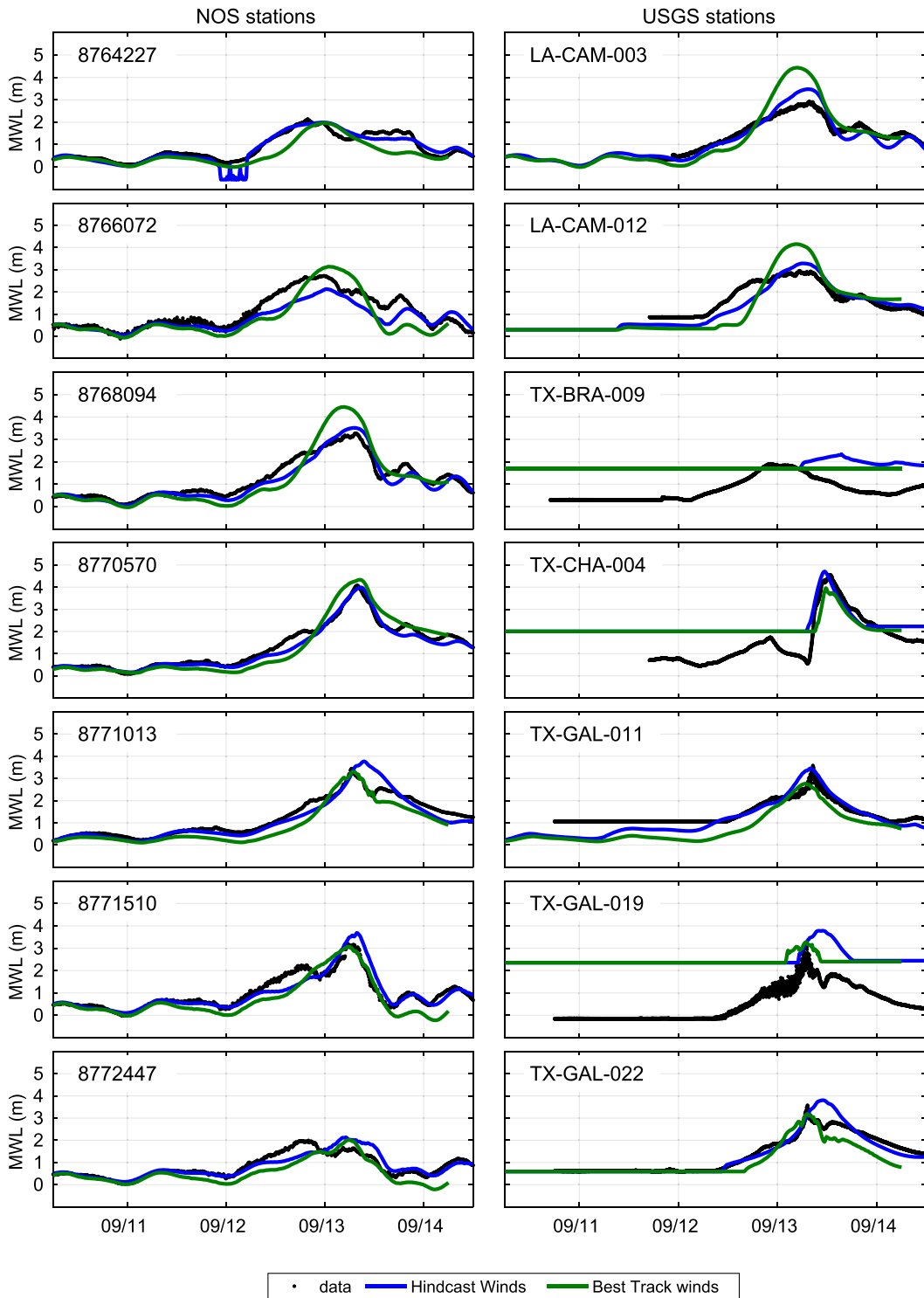
FIG. 8. Water-level comparison between data (black) and hindcast (blue line) and forecast (green line) model results at (left) select NOS stations and (right) at select USGS temporary deployments.
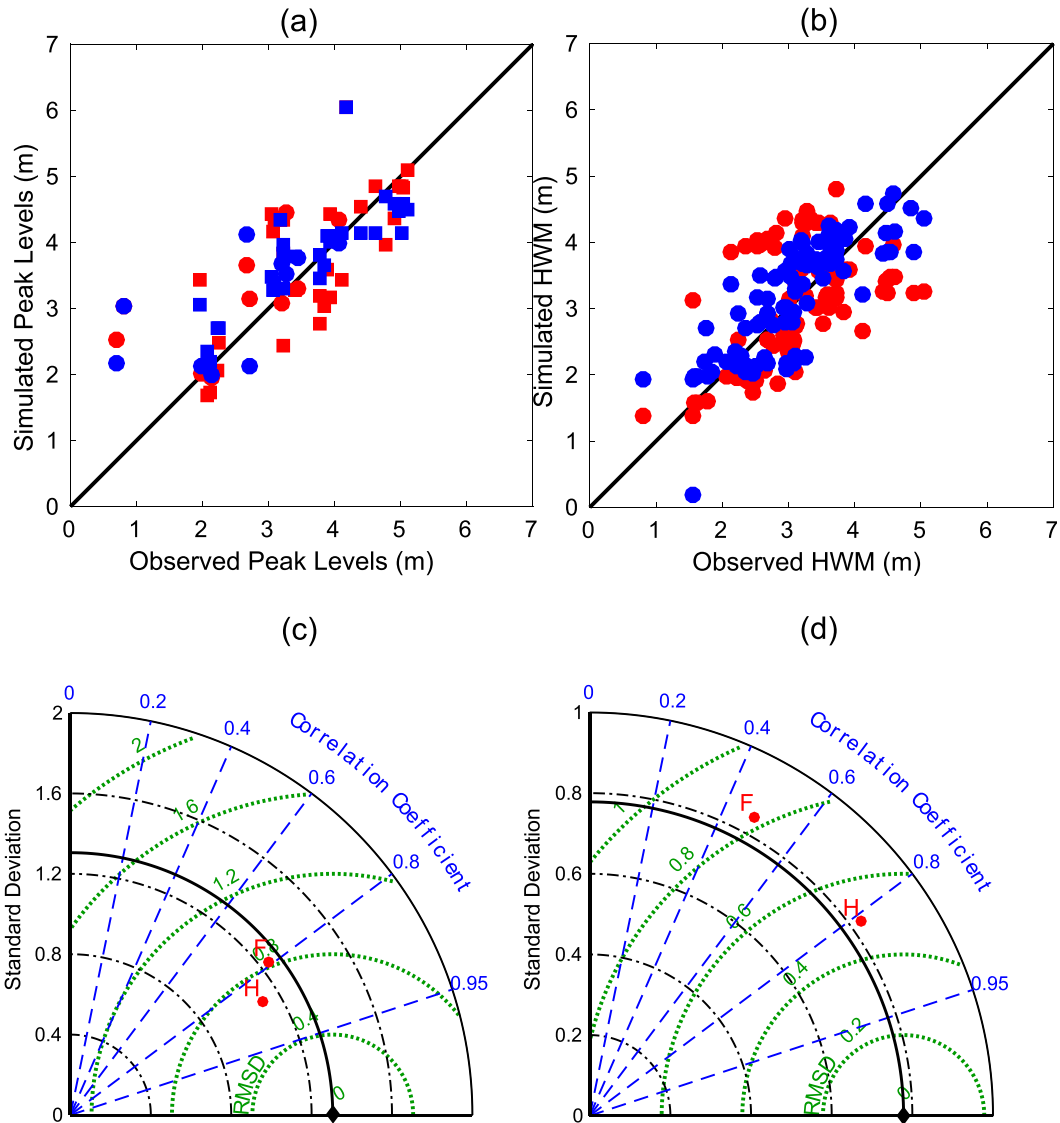
FIG. 9. (a) Simulated vs observed peak water levels at all USGS deployments and NOS stations and (b) HWM comparison using hindcast winds (blue) and forecast winds (red). Taylor diagrams for the (c) USGS stations and (d) NOS stations showing the overall skill using the hindcast winds (H) and forecast winds (F).

were negligibly impacted by the storm. Finally, we looked at the coupling of waves and circulation. In Delft3D, waves can be coupled to the hydrodynamic component using the radiation stress gradient method or the dissipation method. Comparing the results of using the two shows that for low-resolution grids such as that needed for a forecast model the dissipation method works better at reproducing the water levels and inundation. Further research is needed to study the impacts of morphological changes during the event and how such changes affect the surge and inundation. While we used the

analytical wind formulation of Mattocks and Forbes (2008), there may be more appropriate wind models for this particular storm. However, it is difficult to determine a priori which wind formulation to use when developing forecasts. It may be more appropriate to generate forecasts based on ensemble runs with different wind formulations.
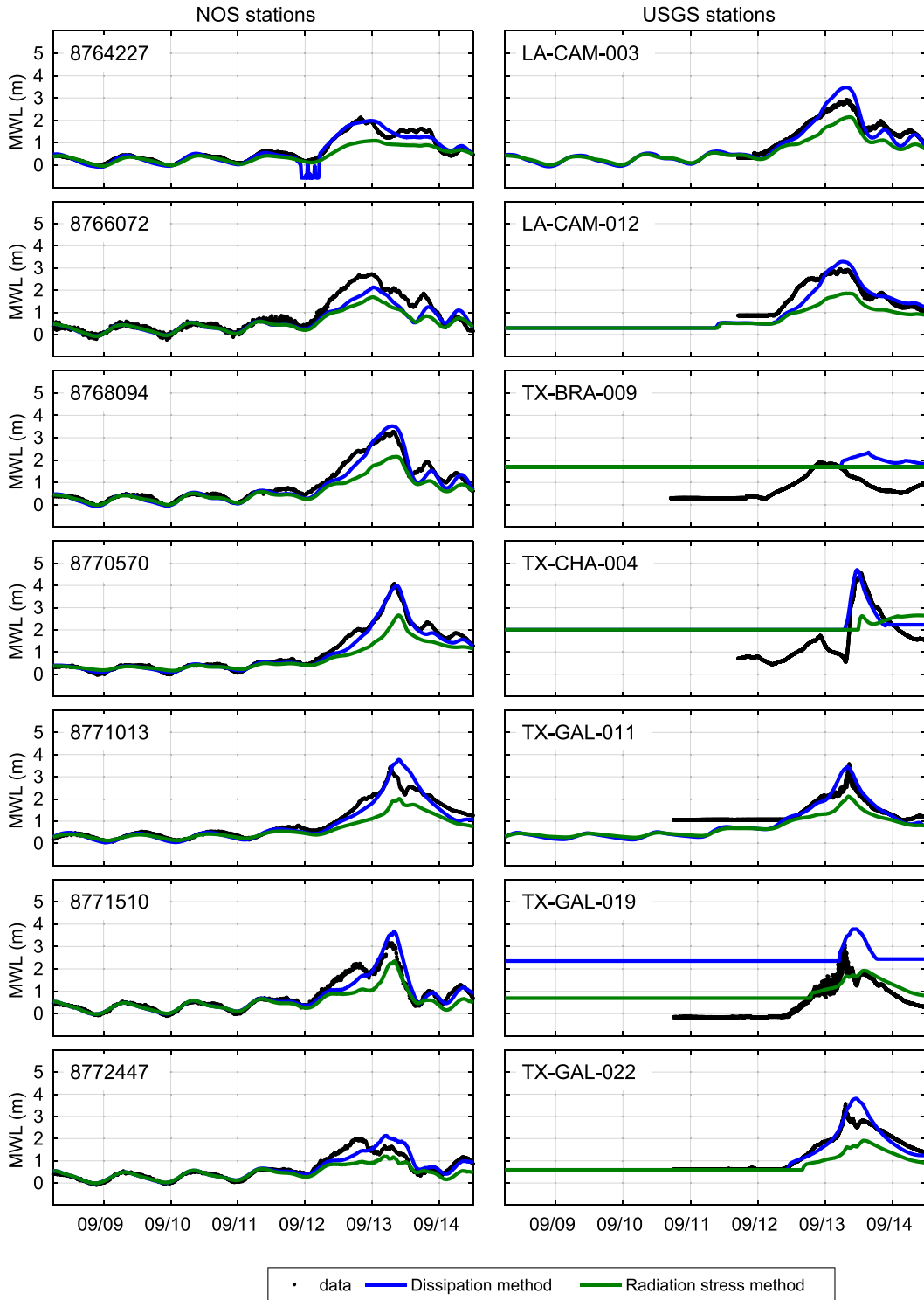
FIG. 10. Water-level comparison between data (black), the dissipation method for coupling (blue), and the radiation stress gradient for coupling (green) at (left) select NOS stations and (right) select USGS temporary deployments.
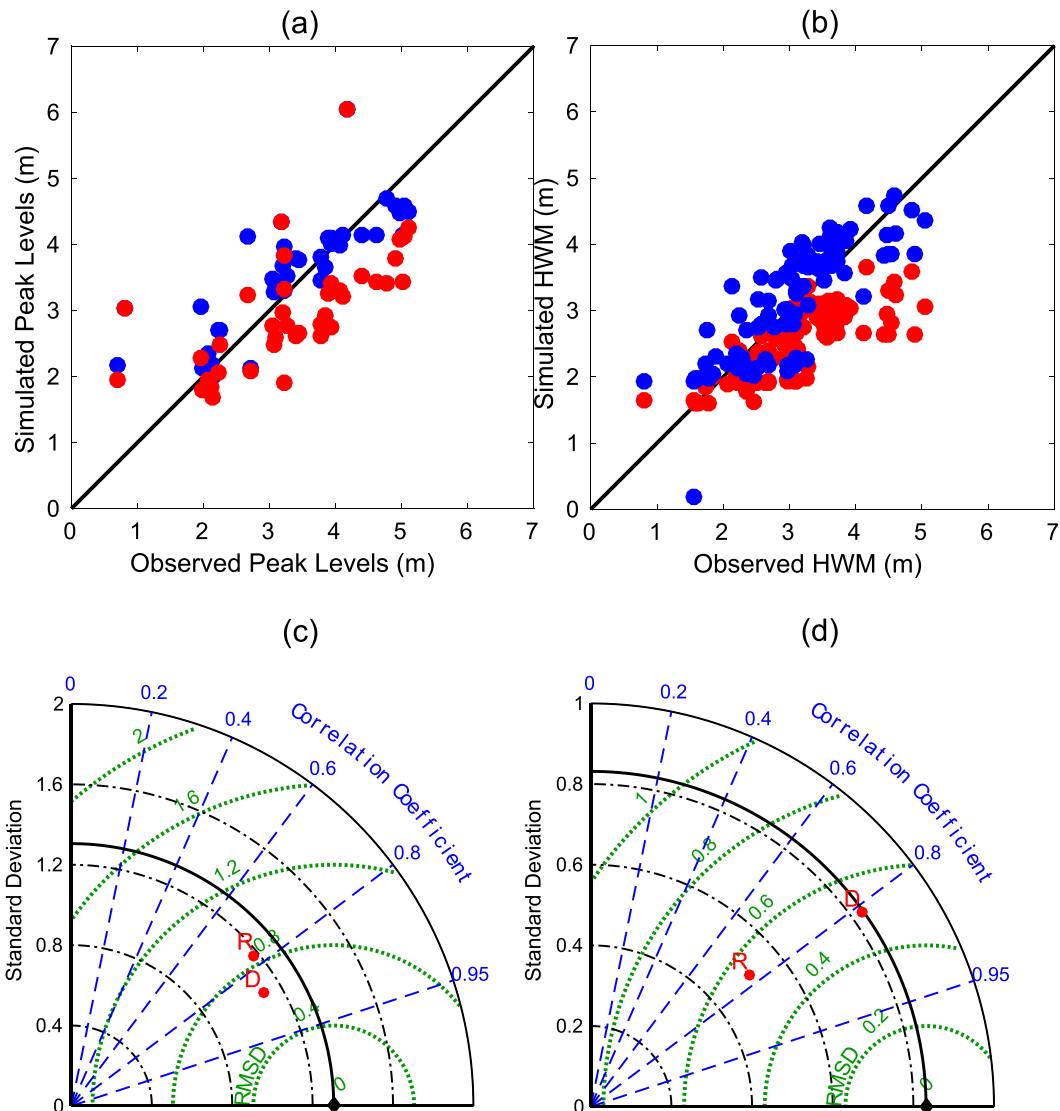
FIG. 11. (a) Simulated vs observed peak water levels at all USGS deployments and NOS stations and (b) HWM comparison using dissipation-based (blue) and radiation-stress-based (red) wave forcing. Taylor diagrams (Taylor 2001) for the (c) USGS and (d) NOS stations, respectively, showing the overall skill using the dissipation method (D) and radiation stress method (R) to compute wave-to-ocean momentum transfer.

REFERENCES

Banner, M. L., and W. L. Peirson, 1998: Tangential stress beneath wind-driven air–water interfaces. *J. Fluid Mech.*, **364**, 115–145, doi:10.1017/S0022112098001128.

Bender, C., J. McKee Smith, A. Kennedy, and R. Jensen, 2013: STWAVE simulation of Hurricane Ike: Model results and comparison to data. *Coastal Eng.*, **73**, 58–70, doi:10.1016/j.coastaleng.2012.10.003.

Booij, N., R. C. Ris, and L. H. Holthuijsen, 1999: A third-generation wave model for coastal regions: 1. Model description and validation. *J. Geophys. Res.*, **104**, 7649–7666, doi:10.1029/98JC02622.

de Boer, G. J., F. Baart, A. Bruens, T. Damsma, P. van Geer, B. Grasmeijer, K. den Heijer, and M. van Koningsveld, 2012: OpenEarth: Using Google Earth as outreach for NCK's data. *NCK-Days 2012: Crossing Borders in Coastal Research*, Enschede, the Netherlands, University of Twente, 97–103, http://proceedings.utwente.nl/177/.

Dingemans, M. W., A. C. Radder, and H. J. de Vriend, 1987: Computation of the driving forces of wave-induced currents. *Coastal Eng.*, **11**, 539–563, doi:10.1016/0378-3839(87)90026-3.

East, J. W., M. J. Turco, and R. R. Mason Jr., 2008: Monitoring inland storm surge and flooding from Hurricane Ike in Texas and Louisiana, September 2008. USGS Open-File Rep. 2008–1365, 34 pp., https://pubs.usgs.gov/of/2008/1365/.

Egbert, G. D., and S. Y. Erofeeva, 2002: Efficient inverse modeling of barotropic ocean tides. *J. Atmos. Oceanic Technol.*, **19**, 183–204, doi:10.1175/1520-0426(2002)019<0183:EIMOBO>2.0.CO;2.

FEMA, 2009: Hurricane Ike in Texas and Louisiana: Building performance observations, recommendations, and technical guidance. Mitigation Assessment Team Tech. Rep. P-757, Federal Emergency Management Agency, 458 pp., https://www.fema.gov/media-library/assets/documents/15498.

Holthuijsen, L., N. Booij, and R. Ris, 1993: A spectral wave model for the coastal zone. *Proceedings of the Second International Symposium on Ocean Wave Measurement and Analysis*, O. T. Magoon and J. M. Hemsley, Eds., American Society of Civil Engineers, 630–641.

Hope, M. E., and Coauthors, 2013: Hindcast and validation of Hurricane Ike (2008) waves, forerunner, and storm surge. *J. Geophys. Res. Oceans*, **118**, 4424–4460, doi:10.1002/jgrc.20314.

Hwang, P. A., 2011: A note on the ocean surface roughness spectrum. *J. Atmos. Oceanic Technol.*, **28**, 436–443, doi:10.1175/2010JTECHO812.1.

Jarosz, E., D. A. Mitchell, D. W. Wang, and W. J. Teague, 2007: Bottom-up determination of air–sea momentum exchange under a major tropical cyclone. *Science*, **315**, 1707–1709, doi:10.1126/science.1136466.

Kennedy, A. B., S. Rogers, A. Sallenger, U. Gravois, B. Zachry, M. Dosa, and F. Zarama, 2011a: Building destruction form waves and surge on the Bolivar Peninsula during Hurricane Ike. *J. Waterw. Port Coastal Ocean Eng.*, **137**, 132–141, doi:10.1061/(ASCE)WW.1943-5460.0000061.

——, and Coauthors, 2011b: Origin of the Hurricane Ike forerunner surge. *Geophys. Res. Lett.*, **38**, L08608, doi:10.1029/2011GL047090.

Kerr, P. C., and Coauthors, 2013a: U.S. IOOS coastal and ocean modeling testbed: Evaluation of tide, wave, and hurricane surge response sensitivities to mesh resolution and friction in the Gulf of Mexico. *J. Geophys. Res. Oceans*, **118**, 4633–4661, doi:10.1002/jgrc.20305.

——, and Coauthors, 2013b: U.S. IOOS coastal and ocean modeling testbed: Inter-model evaluation of tides, waves, and hurricane surge in the Gulf of Mexico. *J. Geophys. Res. Oceans*, **118**, 5129–5172, doi:10.1002/jgrc.20376.

Lesser, G., J. Roelvink, J. van Kester, and G. Stelling, 2004: Development and validation of a three-dimensional morphological model. *Coastal Eng.*, **51**, 883–915, doi:10.1016/j.coastaleng.2004.07.014.

Longuet-Higgins, M. S., and R. W. Stewart, 1964: Radiation stresses in water waves; a physical discussion, with application. *Deep-Sea Res.*, **11**, 529–562, https://doi.org/10.1016/0011-7471(64)90001-4.

Mattocks, C., and C. Forbes, 2008: A real-time, event-triggered storm surge forecasting system for the state of North Carolina. *Ocean Modell.*, **25**, 95–119, doi:10.1016/j.ocemod.2008.06.008.

Oliver-Smith, A., 2009: Sea level rise and the vulnerability of coastal peoples: Responding to the local challenges of global climate change in the 21st century. Interdisciplinary Security Connnections Publ. 7/2009, United Nations University, 52 pp., http://d-nb.info/102969186X/34.

Peng, M. C., L. Xie, and L. J. Pietrafesa, 2004: A numerical study of storm surge and inundation in the Croatan–Albermarle–Pamlico estuary system. *Estuarine Coastal Shelf Sci.*, **59**, 121–137, doi:10.1016/j.ecss.2003.07.010.

Phillips, O. M., 1984: On the response of short ocean wave components at a fixed wavenumber to ocean current variations. *J. Phys. Oceanogr.*, **14**, 1425–1433, doi:10.1175/1520-0485(1984)014<1425:OTROSO>2.0.CO;2.

Powell, M. D., S. H. Houston, L. R. Amat, and N. Morisseau-Leroy, 1998: The HRD real-time hurricane wind analysis system. *J. Wind Eng. Indust. Aerodyn.*, **77–78**, 53–64, doi:10.1016/S0167-6105(98)00131-7.

——, P. J. Vickery, and T. A. Reinhold, 2003: Reduced drag coefficient for high wind speeds in tropical cyclones. *Nature*, **422**, 279–283, doi:10.1038/nature01481.

Rego, J. L., and C. Li, 2010: Storm surge propagation in Galveston Bay during Hurricane Ike. *J. Mar. Syst.*, **82**, 265–279, doi:10.1016/j.jmarsys.2010.06.001.

Ris, R. C., L. H. Holthuijsen, and N. Booij, 1999: A third-generation wave model for coastal regions: 2. Verification. *J. Geophys. Res.*, **104**, 7667–7681, doi:10.1029/1998JC900123.

Rogers, W. E., A. V. Babanin, and D. W. Wang, 2012: Observation-consistent input and whitecapping dissipation in a model for wind-generated surface waves: Description and simple calculations. *J. Atmos. Oceanic Technol.*, **29**, 1329–1346, doi:10.1175/JTECH-D-11-00092.1.

Sheng, Y. P., V. Alymov, and V. A. Paramygin, 2010a: Simulation of storm surge, wave, currents, and inundation in the Outer Banks and Chesapeake Bay during Hurricane Isabel in 2003: The importance of waves. *J. Geophys. Res.*, **115**, C04008, doi:10.1029/2009JC005402.

——, Y. Zhang, and V. A. Paramygin, 2010b: Simulation of storm surge, wave, and coastal inundation in the northeastern Gulf of Mexico during Hurricane Ivan in 2004. *Ocean Modell.*, **35**, 314–331, doi:10.1016/j.ocemod.2010.09.004.

Taylor, K. E., 2001: Summarizing multiple aspects of model performance in a single diagram. *J. Geophys. Res.*, **106**, 7183–7192, doi:10.1029/2000JD900719.

Veeramony, J., M. D. Orzech, K. L. Edwards, M. Gilligan, J. Choi, E. Terrill, and T. De Paolo, 2014: Navy nearshore ocean prediction systems. *Oceanography*, **27**, 80–91, https://dx.doi.org/10.5670/oceanog.2014.70.

Wang, H. V., J. Cho, J. Shen, and Y. Wang, 2005: What has been learned about storm surge dynamics for Hurricane Isabel model simulations? *Hurricane Isabel in Perspective Conf.*, Baltimore, MD, Integration and Application Network, http://www.chesapeake.org/pubs/Isabel/Wang%20et%20al.pdf.

Weisberg, R. H., and L. Zheng, 2008: Hurricane storm surge simulations comparing three-dimensional with two-dimensional formulations based on an Ivan-like storm over the Tampa Bay, Florida region. *J. Geophys. Res.*, **113**, C12001, doi:10.1029/2008JC005115.

Westerink, J. J., and Coauthors, 2008: A basin- to channel-scale unstructured grid hurricane storm surge model applied to southern Louisiana. *Mon. Wea. Rev.*, **136**, 833–864, doi:10.1175/2007MWR1946.1.

Willmott, C. J., 1981: On the validation of models. *Phys. Geogr.*, **2**, 184–194.

Xie, L., L. J. Pietrafesa, and M. Peng, 2004: Incorporation of a mass-conserving inundation scheme into a three-dimensional storm surge model. *J. Coastal Res.*, **20**, 1209–1223, doi:10.2112/03-0084R.1.

——, S. Bao, L. Pietrafesa, K. Foley, and M. Fuentes, 2006: A real-time hurricane surface wind forecasting model: Formulation and verification. *Mon. Wea. Rev.*, **134**, 1355–1370, doi:10.1175/MWR3126.1.

——, H. Liu, and M. Peng, 2008: The effect of wave–current interactions on the storm surge and inundation in Charleston Harbor during Hurricane Hugo 1989. *Ocean Modell.*, **20**, 252–269, doi:10.1016/j.ocemod.2007.10.001.

Zhang, M., and Y. Li, 1996: The synchronous coupling of a third-generation wave model and a two-dimensional storm surge model. *Ocean Eng.*, **23**, 533–543, doi:10.1016/0029-8018(95)00067-4.

Zhang, Y., A. M. Baptista, and E. P. Meyers, 2004: A cross-scale model for 3D baroclinic circulation in estuary-plume-shelf system: I. Formulation and skill assessment. *Cont. Shelf Res.*, **24**, 2187–2214, doi:10.1016/j.csr.2004.07.021.